Nanoscale

Broadband, Self-Biased Photodiode Based on Antimony Telluride (Sb2Te3) Nanocrystals/Silicon Heterostructure

Journal:	*Nanoscale*
Manuscript ID	NR-ART-05-2018-004047.R1
Article Type:	Paper
Date Submitted by the Author:	07-Jul-2018
Complete List of Authors:	Parbatani, Asish; University at Albany College of Nanoscale Science and Engineering, CNSE Song, Eui Sang; State University of New York, College of Nanoscale Science and Engineering Yang, Fan; SUNY Polytechnic Institute, Colleges of Nanoscale Science and Engineering Yu, Bin; State University of New York, College of Nanoscale Science and Engineering

Journal Name

ARTICLE

Broadband, Self-Biased Photodiode Based on Antimony Telluride (Sb_2Te_3) Nanocrystals/Silicon Heterostructure

Received 00th January 20xx,
Accepted 00th January 20xx

DOI: 10.1039/x0xx00000x

www.rsc.org/

Asish Parbatani,[a,b] Eui Sang Song, [a,b] Fan Yang [b] and Bin Yu *[a,b]

Low bulk band-gap and conductive surface electronic states of tetradymites topological insulators (TTI) make them potential candidates for the next generation ultra-broadband photodevices. Here, we demonstrate a broadband and self-biased photodiode based on Sb_2Te_3-Si heterostructure. A low-cost thermal evaporation technique was employed to fabricate the photodiode. The self-biased nature of the photodiode was due to the built-in potential at the Sb_2Te_3-Si interface. Upon characterizing the Sb_2Te_3 nanocrystalline film via AFM, SEM, EDX, and XPS it was found that the film exhibited p-type behavior due to antimony vacancies or antisites. The fabricated photodiode showed excellent rectification ratio of 3388 with n-Si confirming a robust Schottky barrier at the interface and a well-defined photocurrent upon illumination. Due to the p-type behavior of Sb_2Te_3 nanocrystalline film the rectification ratio of only 0.38 was observed with p-Si. The barrier at the interface also increases the carrier lifetimes. Thereby, eliminating one of the biggest drawbacks of ultrafast carrier recombination times in TTI as a photodetection material. Moreover, the photodiode exhibited excellent I_{on}/I_{off} of three orders of magnitude under the self-biased condition, and photocurrents ranging from 520 nm to 980nm wavelengths was observed.

Introduction

Capturing photons and converting them into meaningful electrical signals is widely used in applications like imaging, spectroscopy, optical communications, biomedical imaging etc[1,2,3,4]. With the growing demand for photodevices, it is required for the next generation photodetectors to be broadband, ultrasensitive, high-speed, self-biased, low cost and compatible with the current manufacturing technology[2,5,6,7]. There has been tremendous progress on graphene-based photodetectors in recent years. However, these graphene-based photodetectors have the drawback of large dark currents or scalability issues[8,9,10,11,12]. Another class of layered materials known as transition metal dichalcogenides (TMD) has been studied in recent years which demonstrated excellent photodetection capability[7,13,14,15]. However, slow response time and surface oxidation issues limit these materials towards the practical commercial applications[16,17]. Recently, a new class of materials known as tetradymites topological insulators (TTI) was found to possess excellent photodetection performance[18,19,20,21]. Owing to a narrow band gap (~0.2-0.3 eV)[22,23] and broad wavelength range absorption[24,25, 26] these materials can be employed for ultra-broadband photodetection. Another interesting property of TTI is that its surface states are metallic while the bulk state is semiconducting[27,28,29,30]. These dual electronic states can be tapped for ultra-broadband photodetection application from visible to infrared to terahertz wavelength[31].

Even though TTI have broadband absorption capability the photoconductivity is hard to observe due to ultrafast carrier recombination times and very small carrier lifetimes of 2 ps[32,33,34]. Due to the shorter carrier lifetimes, the majority of photoexcited electron-hole pair recombine before they reach the electrode and therefore very negligible photocurrent is observed at the external circuit and the observed photocurrent is mostly from the carriers intimate to the electrode. One of the ways to overcome this challenge is by introducing a robust Schottky barrier which increases the overall carrier lifetimes[35,19]. The slower relaxation time of carriers is caused due to the band bending at the junction of the Schottky diode, which means the photogenerated carriers are quickly swept across the junction due to the built-in potential. In this paper, we have used our as grown Sb_2Te_3 film on Si which forms a Schottky diode on both n-type and p-type Si. We also compare the photodetection phenomenon and mechanism of Sb_2Te_3/n-Si and Sb_2Te_3/p-Si heterostructure photodiode.

Results and Discussion

Here, we have analyzed the photodetection capability of Antimony Telluride (Sb_2Te_3), which is a low band gap ~0.3 eV[36] TTI material whose surface states are metallic while the bulk is low band gap semiconductor[27]. Figure 1a displays an optical image of the Sb_2Te_3 on Si deposited via low-cost thermal vapor deposition technique. It is noted that Sb_2Te_3 only grows on

[a] State University of New York at Albany, Albany, New York 12203, United States.
[b] SUNY Polytechnic Institute, Albany, New York 12203, United States.
E-mail: byu@albany.edu; Fax: +(518) 956-7492; Tel: +(518) 956-7492
Electronic Supplementary Information (ESI) available: [details of any supplementary information available should be included here]. See DOI: 10.1039/x0xx00000x

open Si window as seen in the optical image (Figure 1a). Sb_2Te_3 is a rhombohedral crystal structure and crystallizes in space group $R\bar{3}m$ with five atoms in a unit cell (Te(2)-Sb-Te(1)-Sb-Te(2))[23]. The Atomic Force Microscopy (AFM) image of as-grown Sb_2Te_3 nanocrystal on Si shows hexagonal morphology (Figure 1b on n-type Si and Figure S1a on p-type Si) which is consistent with the crystal structure of the material. The thickness of the Sb_2Te_3 nanocrystal film was about 250 nm, verified via AFM line-scan information in Figure 1c. The X-ray Photoelectron Spectroscopy (XPS) characterization was also performed on the Sb_2Te_3 film which displays peaks at 532 eV and 538 eV which can be assigned to Sb-3d5/2 and Sb-3d3/2 respectively (Figure 1d). Since Oxygen peak overlaps around 532 eV, we have also measured Sb-3p peaks which could be assigned to Sb-3p3/2 and Sb-3p1/2 for 767 eV and 813 eV binding energies respectively (**Error! Reference source not found.**Figure S1b). The Te-3d5/2 and Te-3d3/2 can be assigned to binding energies of 572 eV and 584 eV respectively (Figure 1e). The EDX spectrum (Figure S1c) of the Sb_2Te_3 nanocrystal film on Si also authenticates that the observed nanocrystals are based off Antimony and Tellurium. The ratio of Sb:Te of 1.91:3.10 was calculated via EDX analysis, validating the presence of Sb vacancies or Sb antisites which are filled by Te. The higher stoichiometric concentration of Te also means the nanocrystal film is p-doped, consistent with the previous reports[37,38,39,40,27,36]. The Raman spectroscopy results show (Figure S1d)) strong peaks at 112.5 cm^{-1} and 166.9 cm^{-1} which can be assigned to E_g (2) and A_{1g} (2) modes respectively[41].

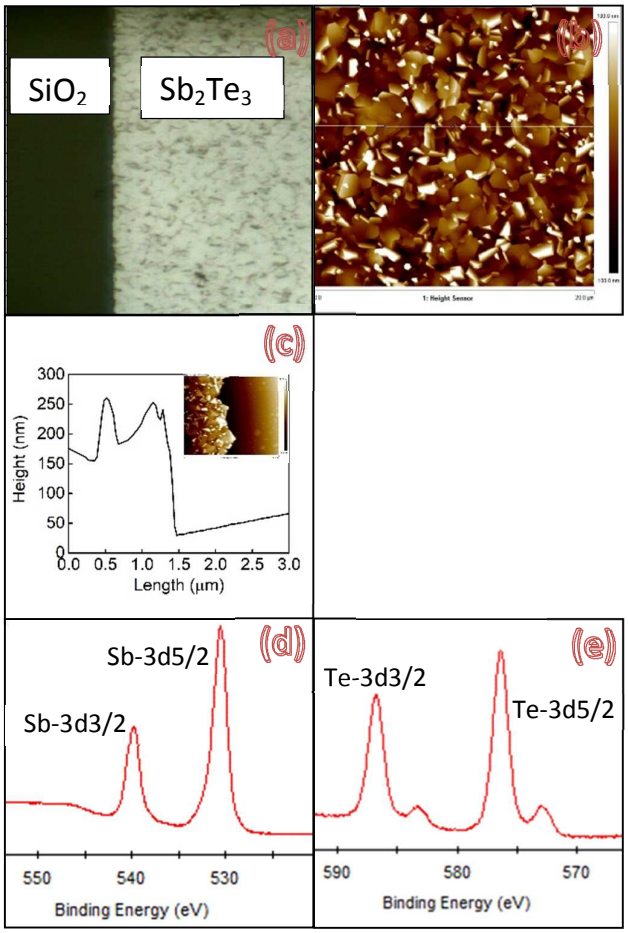

Figure 1: a) Optical image of the Si/SiO_2 substrate post Sb_2Te_3 deposition (Sb_2Te_3 nanocrystals only grow on the Si surface). b) AFM image of the Sb_2Te_3 nanocrystals. c) The plot of the Sb_2Te_3 nanocrystals film thickness.(d,e) XPS analysis of core-level spectra (d) Sb3d (e) Te3d

characteristics of Sb_2Te_3/n-Si and Sb_2Te_3/p-Si heterostructure diode in dark, respectively. The rectification ratio ($RR = I\ (forward\ bias\ V)/I\ (reverse\ bias\ V)$) at 1V for Sb_2Te_3/n-Si and Sb_2Te_3/p-Si heterostructure was calculated to be 3388 and 0.39 respectively. This confirms that Sb_2Te_3/n-Si heterostructure forms an excellent Schottky diode.

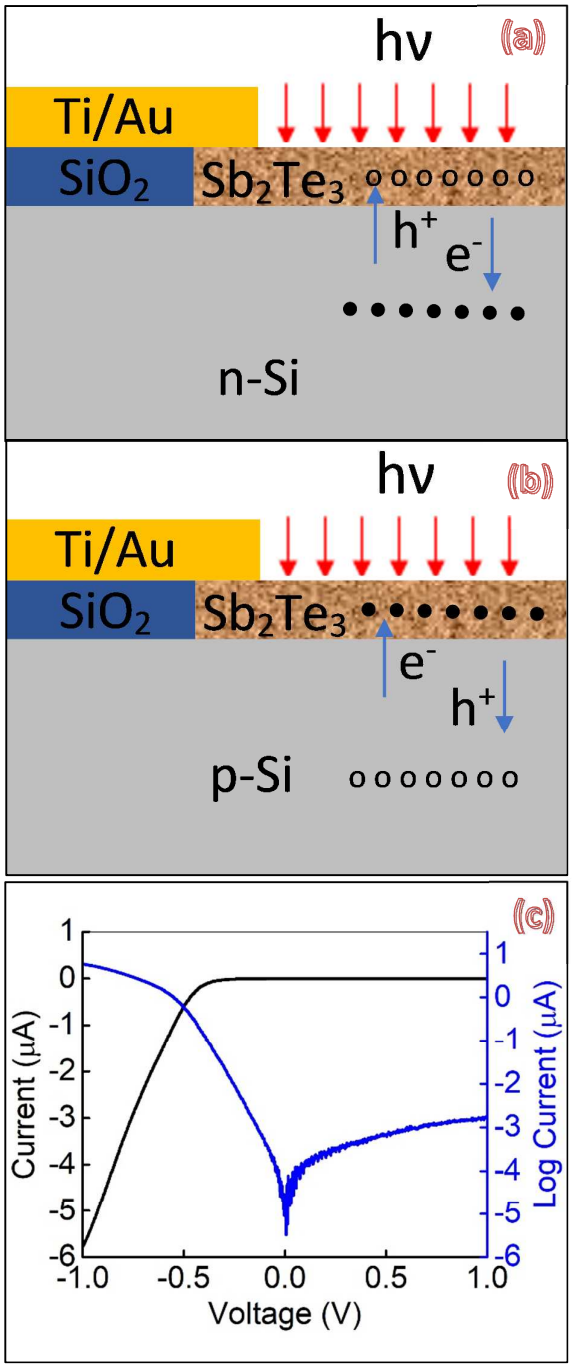

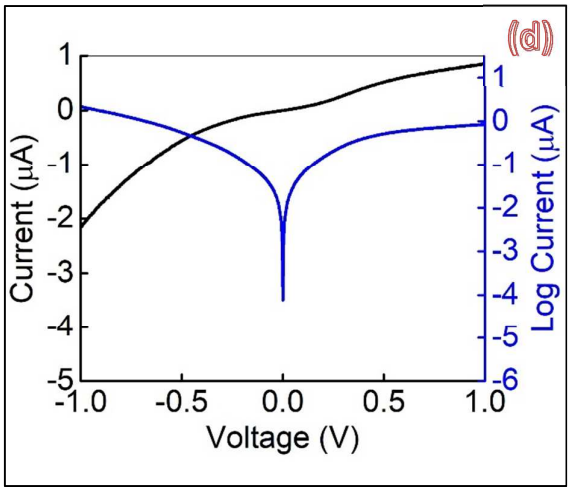

Figure 2: (a) and (b) schematic representation of Sb_2Te_3/n-Si and Sb_2Te_3/p-Si photodiode respectively. (c) and (d) I-V characteristic in Dark (black) and in Semi-logarithmic scale (blue) of Sb_2Te_3/n-Si and Sb_2Te_3/p-Si photodiode respectively.

To assess the photodetection capability of the fabricated photodiodes, we illuminated the devices with light sources of wavelengths 520 nm (Figure S2a-b), 635 nm (Figure 3a-b), and 980 nm (Figure S2a-b). Both n and p-type Sb_2Te_3/Si heterostructure show excellent photodetection capability. The photocurrent was predominantly observed in reverse bias condition for both Sb_2Te_3/n-Si and Sb_2Te_3/p-Si heterostructures (Figure 3a-b). Photocurrent increases linearly with increase in the intensity of the light source as shown in Figure 3c, where dark current (I_{dark}) is the current without light exposure, light current (I_{light}) is the current under light exposure and photocurrent is the light current subtracted from dark current ($I_{photo} = I_{light}$-I_{dark}). This linear increase in the photocurrent with an increase in the intensity of the incident radiation suggests a linear dependence of the electron-hole pair generation with incident photons. The relationship between light intensity and photocurrent can also be demonstrated using power law[21,18] $I_{photo} = AP^{\theta}$, where A is some constant and P is the light intensity and θ demonstrates the exponent factor. The exponent (θ) value of greater than one for both 635 nm and 980 nm (Figure 3d) light source demonstrates higher carrier generation with increase in the light intensity. Figure S2e demonstrates the wavelength and incident power dependent responsivity plot of the Sb_2Te_3/n-Si photodiode. Since, the responsivity of a photodiode is wavelength dependent, it can be improved by optimizing the film thickness. Thin film diodes have better responsivity at shorter wavelengths, as longer wavelengths have higher penetration depth compared to shorter wavelengths.

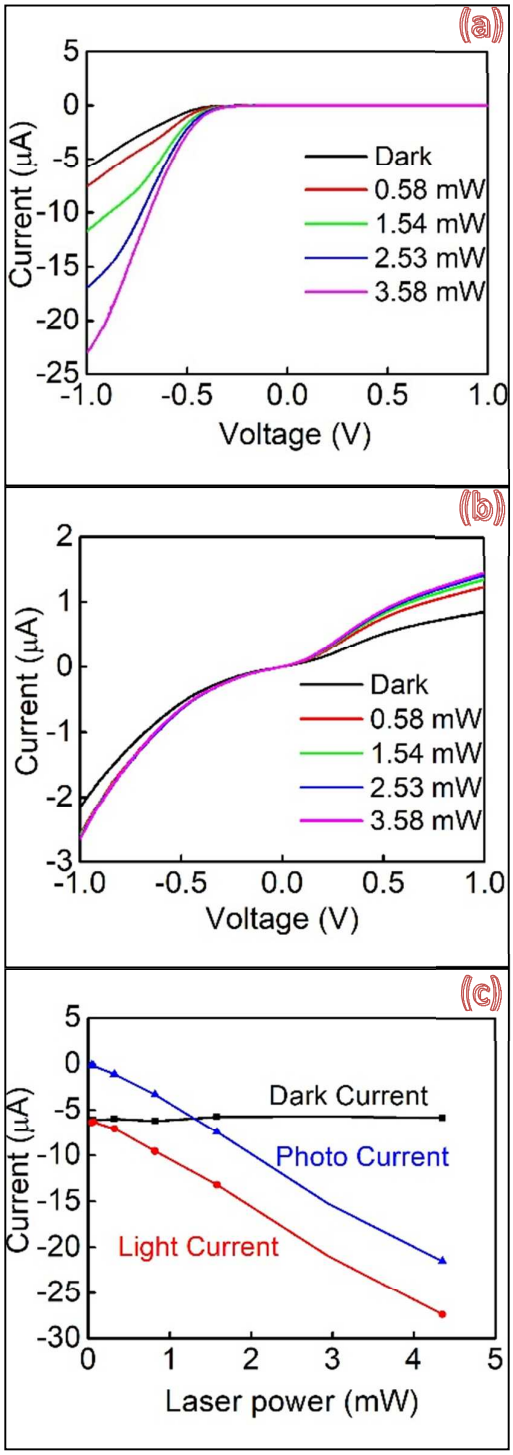

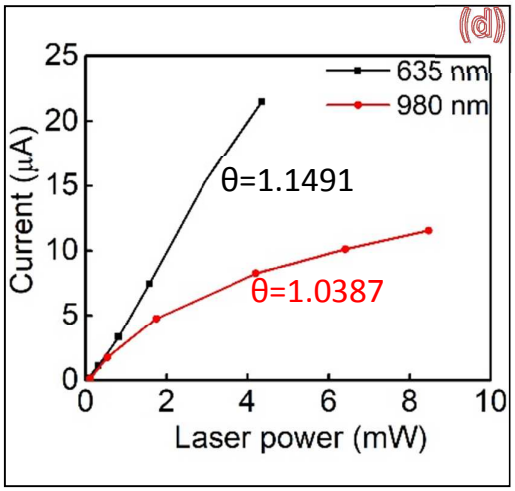

Figure 3: (a) and (b) I-V characteristic measured under 635 nm light source at different intensities for Sb_2Te_3/n-Si and Sb_2Te_3/p-Si photodiode respectively. (c) Plot showing a linear dependence of photocurrent generation with respect to the intensity of the light source. (d) Power law plot of the photodiode illuminated with 635 nm (black) and 980 nm (red) light source.

The photodiode response time is an important figure of merit for evaluating photodetectors. Figure 4a-b illustrate the on/off switching behavior. It is noted that the Sb_2Te_3/Si photodiode is stable for over 1000 cycles. Photocurrent intensifies for both 635 nm (Figure 4a) and 980 nm (Figure S3a) wavelength with an increase in the intensity of the incident radiation suggesting that higher number of the electron-hole pair is generated with an increase in the photon flux. The surge of photocurrent with an increase in the applied bias in reverse bias condition (Figure 4b and Figure S3b) can be attributed to the fact that higher bias creates a steep barrier and therefore many photogenerated carriers are rapidly swept across the junction. A temporal response is a high-frequency measurement of the switching behavior of a photo device. Figure 4c shows the 20 Hz response of the photodiode under pulsed light illumination. We measured the rise (t_r) and fall (t_f) times of 14.22 and 8.2 milliseconds, respectively (Figure S3c). which is much faster than 238.7 and 203.5 seconds reported by Zheng et.al[18] for a Sb_2Te_3 film photodetector. Both Sb_2Te_3/n-Si (Figure 4d) and Sb_2Te_3/p-Si (Figure S3d) diode operate under self-biased condition. Note that spike noise at 10 and 20 seconds is caused due to the fluctuation (increase) in the power of the light source during the switching process. The self-biased nature of the photodiode is due to the photovoltaic effect, where the photogenerated carriers are swept across the junction as a result of built-in potential at the Sb_2Te_3-Si interface. The self-biased photocurrent yielded excellent I_{on}/I_{off} of over three orders of magnitude (Figure S3e). Lower reverse bias saturation current yields higher I_{on}/I_{off} ratio. This reverse bias saturation current is dependent on thermally excited carriers and the number of trap states at the interface of Sb_2Te_3-Si. Therefore, lower the number of trap states higher the I_{on}/I_{off} ratio. Due to the larger reverse bias current of our fabricated photodiode, the I_{on}/I_{off} ratio is lower than that of reported for other TTI/Si heterojuction[19,31,21].

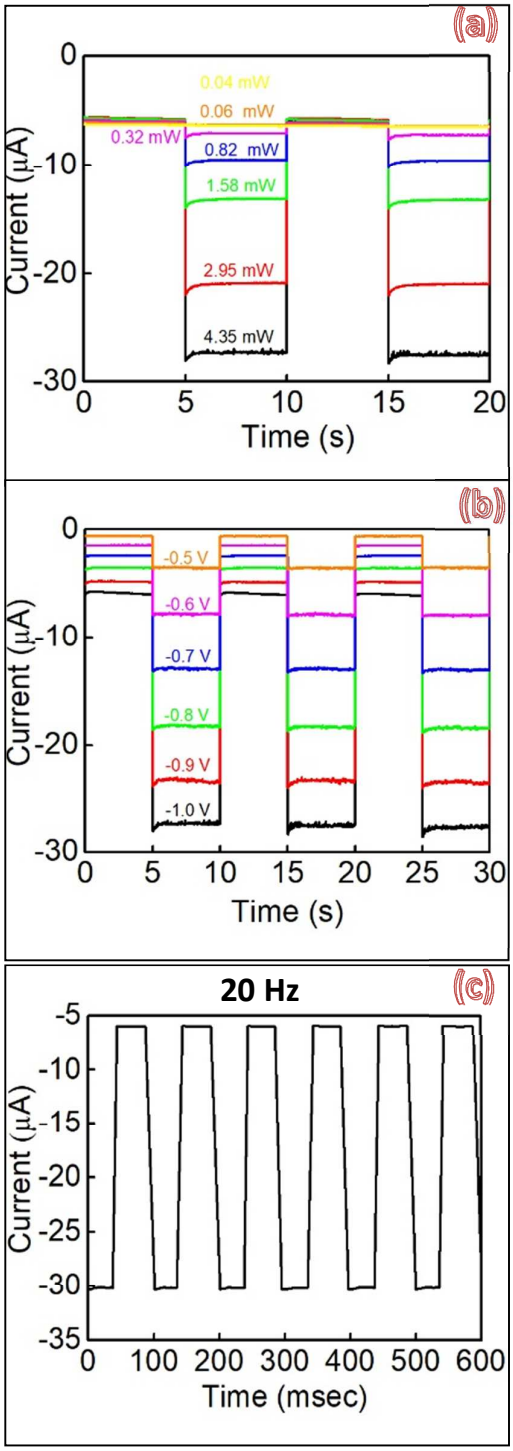

available states for the carriers to occupy. Due to this rapid carrier relaxation time majority of the photogenerated carriers recombine and very little photocurrent is observed. Alternatively, in Sb_2Te_3/p-Si the Si bands bend downwards like a p^+-P junction (Figure 5**Error! Reference source not found.**b). Upon illumination, the photocurrent is also observed in reverse bias. Since in reverse bias, the generated carriers are rapidly swept across the junction facilitated by the steep barrier and higher built-in potential at the interface (Figure S4b). **Error! Reference source not found.** shows the comparison of the recently published photodevices based on TTI. Our Sb_2Te_3/p-Si-based photodiode has a significantly better response time, higher I_{photo}/I_{dark} ratio, self-biased and operates at room temperature compared to Sb_2Te_3 film based photodetector[18].

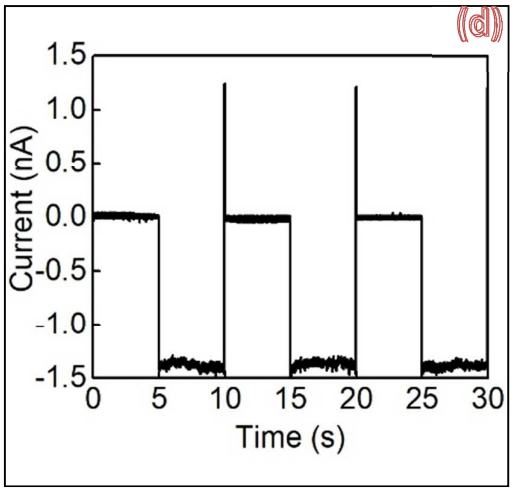

Figure 4: (a) Photocurrent switching behavior of Sb2Te3/n-Si at reverse bias illuminated with 635 nm light source under varying light intensities. (b) Photocurrent switching behavior of Sb2Te3/n-Si illuminated with 635 nm light source at varying reverse bias voltages. (c) Temporal response of the photocurrent switching behavior measured at 20 Hz. (d) The self-biased behavior of Sb2Te3/n-Si photodiode.

Next, we discuss the photocurrent generation mechanism of both photodiodes (Sb_2Te_3/n-Si and Sb_2Te_3/p-Si). Since as grown Sb_2Te_3 nanocrystal film is p-type due to the Sb vacancies, the Fermi level is deduced in the bulk valence band with a bulk bandgap of 0.3 eV[39,27]. When the Sb_2Te_3 nanocrystalline film comes in contact with n-Si, due to the difference in the Fermi level, the Si bands bend upwards creating a space charge region on the Si side (Figure 5a). Upon illumination, the electron-hole pairs are generated in the top Sb_2Te_3 layer and these photogenerated electrons are transported towards the Si creating a current in the external circuit (Figure 5a). In the reverse bias, this process of electron transport towards the Si is facilitated by even steeper barrier height and larger built-in potential (Figure S4a). However, in forward bias, the barrier height is lowered and thereby decreasing the overall built-in potential of the device. This lower barrier height increases the probability of photogenerated carrier recombination and also decreases the

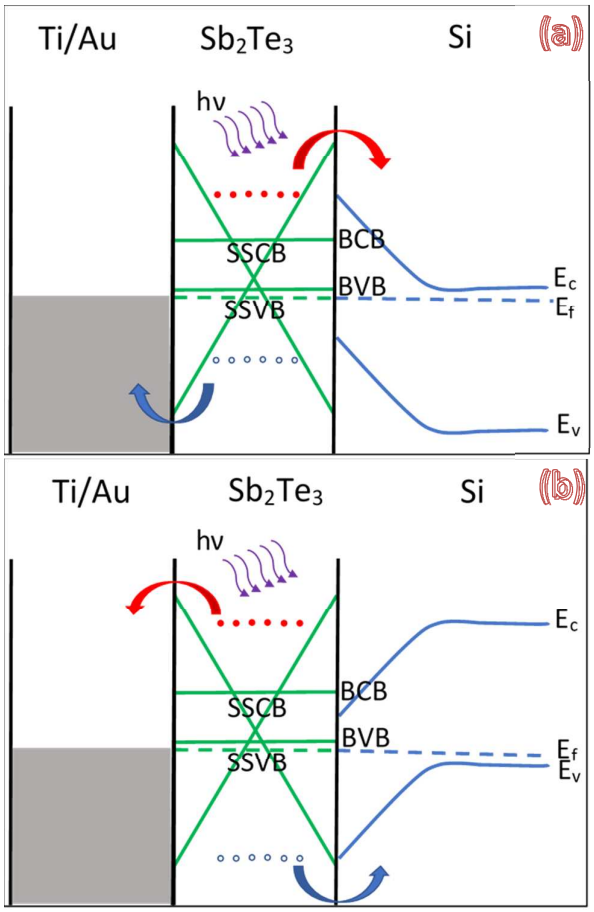

Figure 5: Qualitative illustration of energy band diagram of Sb_2Te_3/Si heterostructure photodiode at thermal equilibrium. BCB, BVB, SSCB, and SSVB are bulk conduction band, bulk valence band, surface state conduction band and surface state valence band of Sb_2Te_3. E_c and E_v are conduction and valence band of Si, E_f is the Fermi level. The band bending and depletion region are not scaled. (a) Schematic illustration of band diagram and photocarrier transport mechanism in Sb_2Te_3/n-Si photodiode under illumination in self-biased condition. (b) Schematic illustration of band diagram and photocarrier transport mechanism in Sb_2Te_3/p-Si photodiode under illumination in self-biased condition.

The Surface topography and the film thickness of Sb_2Te_3 nanocrystal film were characterized using Atomic Force Microscopy (AFM) (Bruker Dimension Icon). Scanning Electron Microscopy (SEM) (LEO 1550 equipped with Gemini column) was utilized to acquire high resolution and magnified images of the nanocrystalline film. The material compositional analysis was performed using Energy-dispersive X-ray spectroscopy (EDS) equipped on LEO 1550 SEM, X-ray Photoelectron Spectroscopy (XPS) (Thermo VG Scientific Theta Probe) and Raman Spectroscopy (Horiba Jobin Yvon HR800). Electrical data was collected using Agilent B1500A Source probe station and to demonstrate the broadband wavelength capability of the photodiode we have used 520 nm, 635 nm and 980 nm light source stocked on Thorlabs MCLS-Series Multi-Channel Fiber-Coupled Laser Source. A high-frequency pulsed light generator (Agilent 33250 Arbitrary Waveform Generator) was used to analyze the photocurrent switching behavior of the fabricated photodetector.

Table 1: Performance comparison of photodetectors based on Sb2Te3 and other TTI based photodevices

TTI material based photodevice	Rectification Ratio	I_{on}/I_{off}	Responsivity (A/W)	Operating condition	Reference
Sb_2Te_3/Si	3388	681	$1.36x10^{-3}$	Room Temperature	This Work
Sb_2Te_3	NA	2.36	21.7	Low Temperatures	18
Bi_2Te_3/Si	~5000	$\sim 1x10^4$	1	Room Temperature	31
Bi_2Se_3/Si	50	$1.55x10^5$	2.6	Room Temperature	19

Experimental

Material Growth

Antimony Telluride (Sb_2Te_3) nanocrystals were grown on Silicon (both n-type and p-type) inside a horizontal 1-inch quartz tube jacketed with a furnace. A quartz boat with two small flakes of high purity (99.999%) Sb_2Te_3 (~150 mg) was placed in the hot center while the substrate was placed 12.5 cm away from the hot center Sb_2Te_3 source towards the vacuum pump line. The upstream end of the tube was connected with Argon gas line while the downstream was connected to the vacuum pump. A low-pressure argon was pumped into the tube for at least 45 min before the growth. The growth was carried at 575^o C with a constant argon flow (~25 sccm) for 3 min. Film thickness could be optimized by adjusting the time, temperature, and gas flow.

Characterization

Device Fabrication Process

Initially, Silicon strips were defined using photolithography process on the SiO_2 (both n-type and p-type) wafer. The exposed SiO_2 was dry etched using CHF_3 gas to create Si/SiO_2 strips substrate. The Si/SiO_2 substrate was then etched with 1% HF for 5 min to minimize the native oxide on the Silicon. After HF etch the substrate was rinsed with acetone and IPA and immediately transferred into our deposition set up. The photodiode was fabricated by deposition of Sb_2Te_3 nanocrystal film on the patterned substrate using the process mentioned above and then the contacts were defined using photolithography process. Finally, Ti/Au electrode (10/50 nm) which forms ohmic contact[18] was deposited using e-beam evaporation technique on top of Sb_2Te_3 nanocrystal film. Ti/Au electrode was used as the top contact while the silicon substrate was used as the bottom contact for I-V characterization.

Conclusions

In summary, we have demonstrated a photodetector based on Sb_2Te_3/Si heterostructure photodiode on both n and p-type Si, which is first of its kind reported at the time of this publication. Our as grown Sb_2Te_3 nanocrystal films exhibited p-type behavior due to the higher stoichiometric concentration of Te. The Sb_2Te_3/n-Si heterostructure showed very high rectification ratio of 3388 proving that Sb_2Te_3 forms a robust Schottky barrier with Silicon. The photodiode displayed room temperature operation and excellent photodetection from visible to near-infrared wavelengths. The self-biased nature of the photodiode originates from the built-in potential between Sb_2Te_3 and Si interface, which also drives the carriers in the opposite direction. The device switching speed of t_r=14.22 and t_f=8.2 milliseconds is much faster than that is reported for Sb_2Te_3 film photodetector. Optimization of film thickness and quality can improve the responsivity of the device and wavelength range. Introducing a light capturing mechanism like antireflection coating can tremendously help overall device performance. This research on Sb_2Te_3 based photodetector paves way for further research on photodetectors based on other TI material as well. Overall, our simple and silicon compatible fabrication process is highly desirable for the large-scale manufacturing process.

Conflicts of interest

"There are no conflicts to declare".

Acknowledgements

We acknowledge SUNY Polytechnic Institute, Miguel Rodriguez for his help with microscopy and Suhasini Gattu for her help with insights on photolithography process optimization.

Notes and references

1 F. H. L. Koppens, DOI:10.1038/NNANO.2014.215.
2 V. Dhyani and S. Das, *Nat. Publ. Gr.*, 2017, 2–10.
3 B. Y. Zhang, T. Liu, B. Meng, X. Li, G. Liang, X. Hu and Q. J. Wang, *Nat. Commun.*, 2013, **4**, 1811.
4 S. C. Dhanabalan, J. S. Ponraj, H. Zhang and Q. Bao, *Nanoscale*, 2016, **8**, 6410–34.
5 D. B. Velusamy, R. H. Kim, S. Cha, J. Huh, R. Khazaeinezhad, S. H. Kassani, G. Song, S. M. Cho, S. H. Cho, I. Hwang, J. Lee, K. Oh, H. Choi and C. Park, *Nat. Commun.*, 2015, 8063.
6 X. Li, L. Basile, B. Huang, C. Ma, J. Lee, I. V Vlassiouk, A. a Puretzky, M. Lin, M. Yoon, M. Chi, J. C. Idrobo, C. M. Rouleau, B. G. Sumpter, D. B. Geohegan and K. Xiao, *ACS Nano*, 2015, **9**, 8078–8088.
7 Y. Gong, J. Lin, X. Wang, G. Shi, S. Lei, Z. Lin, X. Zou, G. Ye, R. Vajtai, B. I. Yakobson, H. Terrones, M. Terrones, B. K. Tay, J. Lou, S. T. Pantelides, Z. Liu, W. Zhou and P. M. Ajayan, *Nat. Mater.*, 2014, **13**, 1135–1142.
8 X. Wang, Z. Cheng, K. Xu, H. K. Tsang and J.-B. Xu, *Nat. Photonics*, 2013, **7**, 888–891.
9 C. C. Cheng, J. Y. Zhan, Y. M. Liao, T. Y. Lin, Y. P. Hsieh and Y. F. Chen, *Appl. Phys. Lett.*, , DOI:10.1063/1.4960357.
10 C. Liu, Y. Chang, T. B. Norris and Z. Zhong, , DOI:10.1038/NNANO.2014.31.
11 T. Mueller, F. Xia and P. Avouris, *Nat. Photonics*, 2010, **4**, 297–301.
12 G. Li, L. Liu, G. Wu, W. Chen, S. Qin, Y. Wang and T. Zhang, *Small*, 2016, **12**, 5019–5026.
13 L. Ye, H. Li, Z. Chen and J. Xu, *ACS Photonics*, 2016, **3**, 692–699.
14 Y. Jiang, L. Miao, G. Jiang, Y. Chen, X. Qi, X. Jiang, H. Zhang and S. Wen, *Sci. Rep.*, 2015, **5**, 16372.
15 S. Yang, C. Wang, C. Ataca, Y. Li, H. Chen, H. Cai, A. Suslu, J. C. Grossman, C. Jiang, Q. Liu and S. Tongay, *ACS Appl. Mater. Interfaces*, 2016, **8**, 2533–2539.
16 W. Zhang, C.-P. Chuu, J.-K. Huang, C.-H. Chen, M.-L. Tsai, Y.-H. Chang, C.-T. Liang, Y.-Z. Chen, Y.-L. Chueh, J.-H. He, M.-Y. Chou and L.-J. Li, *Sci. Rep.*, 2014, **4**, 3826.
17 R. B. Jacobs-Gedrim, M. Shanmugam, N. Jain, C. A. Durcan, M. T. Murphy, T. M. Murray, R. J. Matyi, R. L. Moore and B. Yu, *ACS Nano*, 2014, **8**, 514–521.
18 K. Zheng, L.-B. Luo, T.-F. Zhang, Y.-H. Liu, Y.-Q. Yu, R. Lu, H.-L. Qiu, Z.-J. Li and J. C. Andrew Huang, *J. Mater. Chem. C*, 2015, **3**, 9154–9160.
19 H. Zhang, X. Zhang, C. Liu, S. T. Lee and J. Jie, *ACS Nano*, 2016, **10**, 5113–5122.
20 H. Qiao, J. Yuan, Z. Xu, C. Chen, S. Lin, Y. Wang, J. Song, Y. Liu, Q. Khan, H. Y. Hoh, C. X. Pan, S. Li and Q. Bao, *ACS Nano*, 2015, **9**, 1886–1894.
21 H. Zhang, B. Man and Q. Zhang, *ACS Appl. Mater. Interfaces*, 2017, **9**, 14067–14077.
22 D. Kong and Y. Cui, *Nat Chem*, 2011, **3**, 845–849.
23 R. J. Cava, H. Ji, M. K. Fuccillo, Q. D. Gibson and Y. S. Hor, *J. Mater. Chem. C*, 2013, **1**, 3176.
24 J. D. Yao, J. M. Shao and G. W. Yang, *Sci. Rep.*, 2015, **5**, 12320.
25 W. Zheng, T. Xie, Y. Zhou, Y. L. Chen, W. Jiang, S. Zhao, J. Wu, Y. Jing, Y. Wu, G. Chen, Y. Guo, J. Yin, S. Huang, H. Q. Xu, Z. Liu and H. Peng, *Nat. Commun.*, 2015, **6**, 6972.
26 H. Peng, W. Dang, J. Cao, Y. Chen, D. Wu, W. Zheng, H. Li, Z.-X. Shen and Z. Liu, *Nat. Chem.*, 2012, **4**, 281–286.
27 Y. Jiang, Y. Y. Sun, M. Chen, Y. Wang, Z. Li, C. Song, K. He, L. Wang, X. Chen, Q. K. Xue, X. Ma and S. B. Zhang, *Phys. Rev. Lett.*, 2012, **108**, 1–5.
28 H. Zhang, C.-X. Liu, X.-L. Qi, X. Dai, Z. Fang and S.-C. Zhang, *Nat. Phys.*, 2009, **5**, 438–442.
29 S. Zhu, Y. Ishida, K. Kuroda, K. Sumida, M. Ye, J. Wang, H. Pan, M. Taniguchi, S. Qiao, S. Shin and A. Kimura, *Nat. Publ. Gr.*, 2015, 1–14.
30 Y. C. Arango, L. Huang, C. Chen, J. Avila, M. C. Asensio, D. Grützmacher, H. Lüth, J. G. Lu and T. Schäpers, *Sci. Rep.*, 2016, **6**, 29493.
31 J. Yao, J. Shao, Y. Wang, Z. Zhao and G. Yang, *Nanoscale*, 2015, **7**, 12535–41.
32 J. A. Sobota, S. Yang, J. G. Analytis, Y. L. Chen, I. R. Fisher, P. S. Kirchmann and Z. X. Shen, *Phys. Rev. Lett.*, 2012, **108**, 1–5.
33 M. Hajlaoui, E. Papalazarou, J. Mauchain, G. Lantz, N. Moisan, D. Boschetto, Z. Jiang, I. Miotkowski, Y. P. Chen, A. Taleb-Ibrahimi, L. Perfetti and M. Marsi, *Nano Lett.*, 2012, **12**, 3532–3536.
34 M. Hajlaoui, E. Papalazarou, J. Mauchain, L. Perfetti, A. Taleb-Ibrahimi, F. Navarin, M. Monteverde, P. Auban-Senzier, C. R. Pasquier, N. Moisan, D. Boschetto, M. Neupane, M. Z. Hasan, T. Durakiewicz, Z. Jiang, Y. Xu, I. Miotkowski, Y. P. Chen, S. Jia, H. W. Ji, R. J. Cava and M. Marsi, *Nat. Commun.*, 2014, **5**, 1–12.
35 M. Brahlek, N. Koirala, N. Bansal and S. Oh, *Solid State Commun.*, 2015, **215–216**, 54–62.
36 Y. Jiang, Y. Wang, M. Chen, Z. Li, C. Song, K. He, L. Wang, X. Chen, X. Ma and Q. K. Xue, *Phys. Rev. Lett.*, 2012, **108**, 2–6.

37 S. Jeetendra, N. C. Shivappa, R. Patel and M. H. Matt, *Adv. Mater. Lett.*, 2014, **5**, 639–644.
38 G. Hao, X. Qi, G. Wang, X. Peng, S. Chang, X. Wei and J. Zhong, *RSC Adv.*, 2012, **2**, 10694.
39 L. Plucinski, A. Herdt, S. Fahrendorf, G. Bihlmayer, G. Mussler, S. Döring, J. Kampmeier, F. Matthes, D. E. Bürgler, D. Grützmacher, S. Blügel and C. M. Schneider, *J. Appl. Phys.*, , DOI:10.1063/1.4789353.
40 D. Hsieh, Y. Xia, D. Qian, L. Wray, F. Meier, J. H. Dil, J. Osterwalder, L. Patthey, A. V. Fedorov, H. Lin, A. Bansil, D. Grauer, Y. S. Hor, R. J. Cava and M. Z. Hasan, *Phys. Rev. Lett.*, 2009, **103**, 2–5.
41 G. C. Sosso, S. Caravati and M. Bernasconi, *J. Phys. Condens. Matter*, 2009, **21**, 095410.